ELSEVIER

International Journal of Heat and Fluid Flow 23 (2002) 173–185

International Journal of HEAT AND FLUID FLOW

www.elsevier.com/locate/ijhff

Turbulent heat transfer from a multi-layered wall-mounted cube matrix: a large eddy simulation

B. Ničeno, A.D.T. Dronkers, K. Hanjalić *

Department of Applied Physics, Thermofluids Section, Delft University of Technology, P.O. Box 5046, Lorentzweg 1, 2628 CJ Delft, Netherlands

Abstract

The dynamics of flow and heat transfer on internally heated multi-layered matrix of cubes mounted on one of the walls of a plane channel is investigated by numerical simulation using a finite-volume unstructured solver. The fluid flow and convective heat transfer were solved by large eddy simulation (LES). The temperature field in the cube mantle and on its outer surface – providing the boundary conditions for the convection – was obtained by solving the conduction equation simultaneously with the velocity field. The simulations were performed on the parallel CrayT3E computer at TU Delft using about 425.000 cells clustered around the cube surface and the base wall. The standard Smagorinsky subgrid-scale model was used for LES, with Spalart's adjustment of the filter width in the near-wall region. Comparisons with experiments and with LES on structured orthogonal meshes reported in the literature show good agreement. The temperature distribution on the cube surface was found to be very nonuniform reflecting complex vortex and turbulence structure around the cube. Numerical flow visualisation and animation are used to provide a better insight into the flow pattern and vortex structure and their relation with the local heat transfer and temperature distribution. The configuration considered is relevant to cooling of electronic components on circuit boards or cooling of gas-turbine blades through internal passages equipped with ribs or pins.

1. Introduction

The prediction of local temperature and heat transfer on the surface of wall-mounted bluff bodies in turbulent fluid flow is still a challenge of significant importance in many technological applications. Notable examples are electronic components attached to a printed circuit board in electronic equipment. With a concentrated power dissipation, these components act as strong local heat sources which may cause excessive local overheating so that efficient heat removal is the crucial prerequisite for a reliable long-term operation. A continuous tendency towards the component miniaturisation and ever-increasing unit power pose new challenges to optimum design, which must rely on accurate predictions of local heat transfer (Lasance, 1997). Similar problems are encountered in gas turbines where the desire to improve engine efficiency leads inevitably to an increase in the temperature of the combustion gases. Contemporary turbine blades are usually cooled by cold fluid circulation through internal passages equipped with wall-mounted protruding ribs and pins (Baughn and Yan, 1992). Inefficient cooling can lead to local blade overheating, which may cause permanent damage and a shortening of the blade life time. In both examples, as well as in many other applications, predicting accurately the local temperature and heat transfer is the key prerequisite for successful design and for ensuring reliable equipment functioning.

The structure of flow around a surface-mounted bluff body depends, of course, on the shape and relative dimensions of the body. However, in most cases the flow is characterised by a typical pattern with fluid impingement and formation of a wrapping horse-shoe vortex on the front face, separation and vortex shedding on the sides and behind the body, with several recirculation regions. The rate of total convective heat transfer from a heated body to the surrounding fluid is proportional to the average fluid velocity and the average temperature difference between the solid surface and the fluid. However, the local heat transfer is highly dependent on the immediate flow structure around the obstacle.

* Corresponding author. Tel.: +31-15-278-1735; fax: +31-15-278-1204.

E-mail addresses: hanjalic@ws.tn.tudelft.nl, hanjalic@duttwta.tn.tudelft.nl (K. Hanjalić).

0142-727X/02/$ - see front matter
PII: S0142-727X(01)00147-3

Generally, heat transfer is enhanced on the front face in the impingement zone, where heat is being removed and carried away by the wrapping horse-shoe vortex. Flow separation and reattachment are also associated with a local increase in heat transfer mainly due to high turbulence generated in the separation shear layers. However, the fluid trapped in recirculating regions on the sides and behind the body undergoes local heating, reducing thus the effective temperature difference between the fluid and the body and diminishing the overall heat transfer on the body surfaces. Flow instability leads to vortex shedding at the sides and rear face of the obstacle, which imposes unsteadiness and quasi-periodicity in the whole flow domain even if the flow is steady in the bulk. If the Reynolds number is not high, turbulence often remains isolated in patches in the shear layer around the protrusion, while the flow further away remains more or less undistorted. All these phenomena lead to steep spatial and temporal gradients in the distributions of the local temperature and convective heat transfer. In short, such a complex vortical structure imposes strong nonuniformity in heat transfer with possible local overheating and hot spots, which can cause malfunctioning of cooled engineering appliances. For example, it is generally believed that local overheating in integrated electronic circuits is the major cause for the technical failure of electronic equipment.

In order to provide reference data on flow and heat transfer around surface-mounted protrusions relevant to electronics circuitry, with well-defined and reproducible inflow and boundary conditions, Meinders and Hanjalić (1999) (see also Meinders, 1998) investigated experimentally a matrix of equidistant cubes mounted on one of the walls of a plane channel. An internally heated cube was placed in the middle of the matrix of identical but nonheated cubes, all mounted on a constant temperature channel wall. The surrounding cubes in the matrix ensured a fully developed situation with periodic boundary conditions, suitable for numerical simulations. Although far from the real configuration of an electronic board or turbine blade internal cooling passage, the investigations of this generic flow cases provided useful data and insight into the physics of the flow structure, turbulence and heat transfer, which can be used for the design optimisation of real engineering problems. Using laser Doppler anemometry (LDA) for measuring velocity field, infrared thermography and liquid crystals for surface temperature measurements, and flow and surface visualisation, Meinders and Hanjalić (1999, 1998) provided a comprehensive data set and sufficient evidence to construct the typical pattern of the flow structure and its relation with the local distribution of the heat transfer coefficient on the cube surface. A two-cell structure in the immediate proximity of the cube was detected, caused by the shear layer reattachment in the inter-obstacle space. The horse-shoe vortex in front of the cube and an arch vortex behind it, the latter attached with both legs to the base plate, were clearly identified. Elongated vortices were detected on each side of the cube close to the leading edge, attached on one side to the cube faces and on the other to the base wall. A thin confined recirculation bubble also appeared on the cube top face close to the leading edge. This pattern is well reflected in the distribution of the heat transfer and surface temperature. Regions of intense flow recirculations showed relatively small values of the local heat transfer coefficient. Large values of the heat transfer coefficient were found in areas where the flow separates and reattaches.

These experimental results served as reference data for validating the computational modelling and simulation in the 6th and 8th ERCOFTAC/IAHR/COST Workshops on refined flow and turbulence modelling (Delft, 1997 and Helsinki, 1999), see e.g. Hanjalić and Obi (1997, 1999). Several computations with the Reynolds-averaged Navier–Stokes (RANS) method with different turbulence models were presented, but none was satisfactory. One of the reasons was that all computations considered the flow as being steady. Without proper evidence it is difficult to judge how an unsteady RANS would perform, but the common feature of all computations was the inability to capture the high peaks of turbulence second moments in the thin shear layers around the cube, a failure which can also be associated with a lack of numerical resolution. In contrast, large eddy simulations (LES) presented by three groups all showed satisfactory agreement (Van der Velde et al., 1999; Mathey et al., 1999; Ničeno and Hanjalić, 1999).

Van der Velde et al. (1999) computed this flow without using any subgrid-scale turbulence model, thus performing a kind of direct numerical simulation (DNS) on a grid which does not fully meet the required resolution criteria for true DNS. The computation domain was covered by an orthogonal 100^3 grid, clustered towards the solid walls. Time-averaged results were computed over (at least) 16 shedding cycles. The profiles of both velocity field and temperature were found to be in good agreement with experimental results. Mathey et al. (1999) reported a large eddy simulation using also a Cartesian grid with 100^3 grid points, clustered towards the cube and channel walls. The computed temperature distribution along the cube faces showed mostly good agreement with experiments, though close to the lower channel wall the temperature was somewhat overpredicted. Ničeno and Hanjalić (1999) presented large eddy simulations using an unstructured grid with 418,760 cells. Only the mean and fluctuating velocity fields were calculated, i.e. without heat transfer. The profiles matched well with the experimental data. The use of an unstructured grid led to a significant reduction in the number of computational cells, less than half com-

pared with simulations on structured orthogonal grid reported in Van der Velde et al. (1999) and Mathey et al. (1999).

In this paper we present a numerical simulation of the turbulent flow and conjugate heat transfer for the same configuration. A large eddy simulation was performed to compute the velocity and temperature fields in fluid flow around the cubes, whereas the temperature field in the low-conductivity mantle and on its outer surface – providing the boundary conditions for heat convection – was obtained by solving the conduction equation simultaneously with the velocity field. The major difference from numerical simulations reported in Mathey et al. (1999) and Van der Velde et al. (1999) is the use of an unstructured finite-volume solver and unstructured computational grid. Although the shape of grid cells adopted is, for convenience, still hexahedral, any type of cell shapes can be used. The details of the solver and illustration of simulations of some simple generic flows with several different grids are reported by Ničeno and Hanjalić (submitted). The major advantage of the unstructured grid is in its potential to treat very complex flow domains and body shapes, as well as to achieve the desired local grid refinement where it is needed, with a relatively small total number of grid points. This allows LES at relatively high Reynolds numbers with an affordable computational effort. The unstructured solver permits a decrease in the number of cells by choosing an appropriate mesh to fit the body shape, i.e. nonorthogonal cells enveloping the body with local clustering and refinement towards the solid walls, without a significant loss of accuracy.

Results are presented for the mean velocity and temperature fields, second moments of the turbulence field and heat transfer on the cube. The results are generally in very good agreement with the experiments. In addition to verification of the experimental results, LES provides further information, which are inaccessible to experiments either because of the inability to measure some flow properties or because of insufficient resolution in all flow areas of interest. Especially useful are the time-dependent results which enable the instantaneous flow patterns and their time evolution to be studied, as well as the identification of coherent structures and their dynamics. Vortical structures in the immediate vicinity of the cube, detected by experiments, have now been confirmed by LES and can be correlated with the instantaneous temperature field on the cube surface. This, in turn, enables the local hot spots that appear as a consequence of locally trapped fluid in recirculation zones to be detected and identified, particularly on the cube rear face. In contrast to experiments, LES also enables numerical flow visualisation and animation, which provide very good insight into the eddy structure and its relation to the local heat transfer and temperature distribution.

2. Computational set-up and numerical details

2.1. Flow configuration

The problem domain consisted of a single heated cube in an equidistantly spaced matrix of wall-mounted cubes placed on the floor of a rectangular high-aspect-ratio wind-tunnel section. The dimension of the cubes was h^3 and the height of the channel was $D = 3.4h$. The distances between the cubes were $3h$, giving centre-to-centre distances of $S_x = S_y = 4h$. A sketch of the set-up is shown in Fig. 1. The x, y and z directions are in the streamwise, spanwise and normal direction, respectively. The computational domain consisted of a subchannel unit of dimension ($4h \times 4h \times 3.4h$), encompassing the cube that was placed in the domain centre, as illustrated in Fig. 1. The spatial periodicity in both streamwise and spanwise directions allowed to apply periodic conditions for the velocity at the boundaries of the computational domain. On the channel floor and top wall, no-slip conditions were applied. Since the simulations were aimed at reproducing the experiment, we considered a single heated cube placed in a matrix of nonheated cubes, so that the periodic boundary conditions could not be applied to the temperature. Instead, the temperature of the incoming fluid was fixed to $T_{\mathrm{ref}} = 20$ °C. At the domain outlet the normal derivative of temperature was assumed to be zero. The cubes were mounted on a base plate at constant temperature equal to the temperature of the incoming fluid. On the join of the heated cube and the floor the Neumann boundary condition was applied with zero heat flux. The heated cube consisted of a constant-temperature core covered with a thin epoxy mantle of thickness $0.1h$ with a low thermal conductivity of 0.24 W/m K. The inner side of the epoxy layer was set to a constant temperature of the cube core

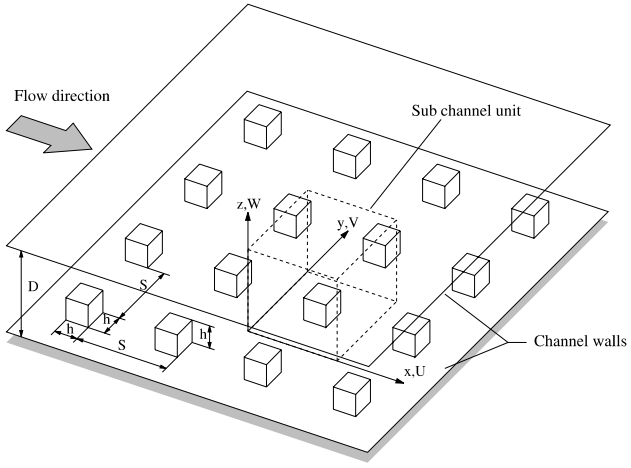

Fig. 1. Schematic picture of the configuration of the wall-mounted matrix of cubes.

Table 1
Set-up dimensions and material properties

D	Channel height	$3.4h = 51$ mm	
S_x, S_y	Centre-to-centre distances	$4h = 60$ mm	
T_c	Imposed cube-core temperature	75 °C	
T_{ref}	Reference temperature	20 °C	
h	Dimension of the cubes	15 mm	
δ_e	Epoxy layer thickness	1.5 mm	
		Air	Epoxy
c_p	Specific heat (m^2/s^2 K)	1007.0	1668.5
α	Thermal diffusivity (m^2/s)	2.197×10^{-5}	1.230×10^{-7}
λ	Thermal conductivity (kg m/s^3 K)	0.0257	0.236
ν	Viscosity (m^2/s)	1.567×10^{-5}	–
ρ	Density (kg/m^3)	1.16	1150.0

$T_c = 75$ °C during whole simulation. The temperature distribution in the epoxy layer is determined by the inside temperature T_c and the surface temperature T_s. The latter was obtained by simultaneous solution of unsteady heat conduction through the epoxy layer and heat convection in the fluid. This coupling of the temperature fields and computation of the instantaneous cube surface temperature T_s is one of the major outcomes of the present simulation. The computations were performed at a Reynolds number of $Re_D = U_0 D/\nu = 13{,}000$, corresponding to a Reynolds number based on the cube height of $Re_h = 3854$, and with $Pr = 0.712$ (air). To obtain this value, the bulk velocity was set to $U_0 = 3.86$ m/s yielding the mass flux per subchannel $\dot{m} = 13.70 \times 10^{-3}$ kg/s. All relevant dimensions and physical properties (taken from the experimental report Meinders, 1998) are summarised in Table 1.

2.2. Computational grid and numerical procedure

The use of an unstructured grid is expected to rationalise grid distribution which will permit the use of a significantly smaller number of grid cells than that required by the structured grid for a similar near-wall resolution. A moderate number of grid cells was adopted with 427,680 cells (373,248 cells in the outer region and 54,264 cells for the epoxy layer). Figs. 2(a)–(c) show the computational grid. The presence of the solid boundary affects the physics of the subgrid scales in several ways: the growth of the small scales is inhibited by the presence of the wall, the exchange mechanisms between the resolved and unresolved scales are enhanced, and the subgrid scales in the near-wall region may contain some significant Reynolds-stress producing events (Piomelli, 1997). In order to account for these mechanisms the wall

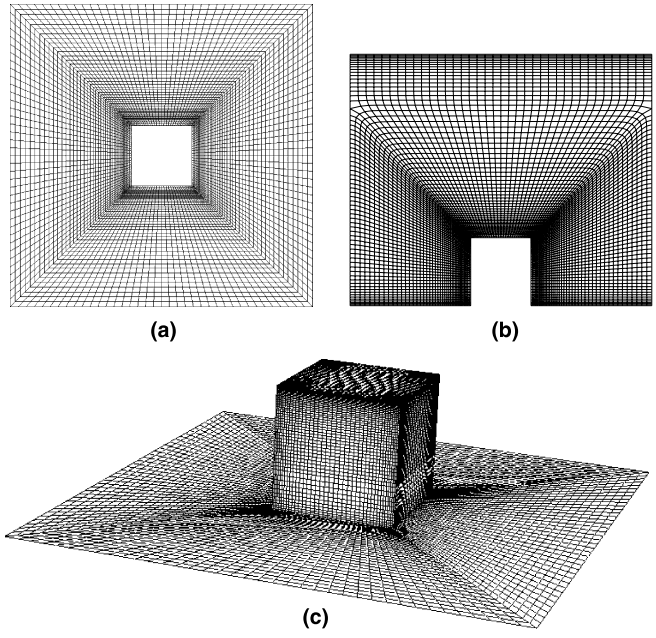

Fig. 2. Computational grid: top view (a), side view (b) and perspective view (c) of the unstructured mesh.

region is resolved by clustering the mesh hyperbolically towards the walls and edges in such a way that the first calculation point was at a location $0.006h$. For the considered Reynolds number this corresponds to $y^+ \approx 1$ for channel flow without a cube. The wall-nearest y^+ around the cube was roughly of the same order of magnitude.

In order to prevent high-aspect-ratio cells near the wall, with consequent degradation of the resolution and numerical accuracy, the grid spacing in the streamwise and spanwise directions was limited to be $<0.032h$ (which is found to be sufficient for LES, Piomelli, 1997). This corresponds to the dimensionless streamwise and spanwise spacings Δx^+ and Δz^+ less than six for a channel flow, though somewhat larger values were detected on the cube. The cube surface mantle (epoxy layer), indicated in Fig. 2, was covered by 38 cells in each direction, with six cells across the epoxy layer thickness. These cells were also clustered towards the edges and outer boundary of the cube, in order to have approximately the same cell sizes at the fluid–solid interface.

A large eddy simulation was performed with the Smagorinsky model for the subgrid stresses. The Smagorinsky constant is set to $C_S = 0.1$. No wall function was used. In order to reduce the excessive eddy viscosity in the near-wall regions, the filter width is defined as the minimum between the cubic root of the cell volume and the distance to the nearest wall (Spalart et al., 1995):

$$\Delta = \min[(V)^{1/3}, \delta], \tag{1}$$

where V is the cell volume, and δ is the distance to the nearest wall. The numerical simulations were performed using the in-house computer code T-Rex. The discretisation of the governing equations is based on the finite-volume method for an unstructured grid. Central differences were used for the diffusive and convective terms, with underrelaxation of the pressure and temperature fields by factors of 0.6 and 0.8, respectively. A small percentage of upwinding (<3%) was found beneficial for stability of the computations. The time marching was performed using a fully implicit three-level time scheme. The time step was set to $\Delta t = 0.0015$ and was kept constant during the calculations. The maximum CFL number was 1.4–1.9, observed only locally in regions of high velocity around cube edges, whereas the typical value in most areas was around 0.6. More details on the numerical method used have been reported in Ničeno and Hanjalić (submitted).

The simulations were conducted on the parallel Cray T3E computer at TU Delft using 16 processors. Since each processor was assigned its own subdomain, the computational domain was decomposed into 16 equally balanced subgrids. Each subgrid was saved to a separate file as an independent identity. These separate files allowed a parallel input/output. The simulations were started from the uniform flow field ($U_0 = 3.86$ m/s) and constant mass flux $\dot{m}_0 = 13.70 \times 10^{-3}$ kg/s in the entire domain. In order to enhance turbulence, the flow field was perturbed by random fluctuations with an amplitude of 10% of the streamwise velocity component. This was done only in the initial stage of the calculation. As it follows from Table 1, the ratio of thermal diffusivities for air and the cube's epoxy layer is $\alpha_{air}/\alpha_{epoxy} \approx 180$. This ratio is equivalent to the characteristic time-scale ratio of the temperature evolution in the fluid and the solid. Using this ratio with initially a uniform field would require a long time before reaching a statistically stationary state in the epoxy layer. Therefore, the ratio was set initially to $\alpha_{air}/\alpha_{epoxy} = 20$ (by increasing the thermal diffusivity of the epoxy) at the start of the simulation, and was gradually increased during the computations. Gathering the results for the evaluation of the statistics was started only after the proper value for α_{epoxy} was introduced.

The SIMPLE algorithm was used for coupling velocities and pressure. In order to keep the mass flux constant through the domain, the pressure drop was recalculated after each time step, as a difference between the imposed mass flux $\dot{m}_0$ and the calculated one $\dot{m}$. The calculated mass flux changed from one time step to another, resulting in a varying Reynolds number. However these variations were quite small, ≈0.02%.

The gathering of the statistics started at time step 15,000 and continued until time step 50,000. Meinders and Hanjalić (1999) calculated the dominant characteristic wake frequency from the maximum energy in the power density spectrum, which was obtained from 20,000 to 40,000 vortex shedding cycles. For this case ($Re_h = 3854$), the dominant frequency was found to be $f = 27$ Hz, yielding the Strouhal number $St = 0.109$ (based on the cube height h and incoming bulk velocity U_0). From this value, we can conclude that the time averages were computed over about 35 shedding cycles.

3. Results

Before comparing the LES results with measurements and discussing specific flow properties and heat transfer, we consider first the morphology of the flow structure and its role in local heat removal from the cube. The general flow patterns with distinct vortical structures in the immediate proximity of the cube were detected by experiments, but many more details of this complex structure organisation have been revealed by LES. In this section we provide a description of these structures both for the averaged field and its time evolution, based on LES. This is followed by a comparison of the velocity profiles with the experiments. Finally the convective heat transfer from the heated cube to the surrounding flow is analysed.

3.1. Flow structures

The streamline plots for the time-averaged velocity field and the corresponding temperature field in the vertical z–x mid-plane at $y/h = 2.0$, and in the horizontal x–y plane very close to the base wall at $z/h = 0.006$, respectively, are given in Fig. 3. For better clarity the streamlines are visualised over two adjacent subchannel units. As expected, distinct vortex structures were observed only in the immediate proximity of the obstacle. Fig. 3(a) shows two main vortex structures: a large curled recirculation in the proximity of the windward cube face and a recirculation in the wake of the cube. The approaching fluid impinges on the front face of the cube. The stagnation point is located at approximately $z/h = 0.8$. The flow beneath this stagnation point collides with the wall, creating a high pressure region which results in a downwash of the flow close to the wall ending in the recirculation zone in the form of a horse-shoe vortex. Due to the downwash, high heat transfer from the cube into the flow is induced and heat is transported into the vortex.

In the wake, another recirculation, bounded by the shear layer can be discerned. This vortex causes a strong upwash close to the rear wall. In combination with the horse-shoe vortex this upwash scrapes heat from the wall, but the heat remains trapped in the recirculation zone, as illustrated by the reduced temperature gradients in these zones, Fig. 3. The shear layer, which originates from the flow separation at the sharp leading edge of the top face, is curled towards the base wall. The flow reattachment at the channel floor occurred approximately mid-way between the cubes at $x/h = 4.0$. This is fully in accord with experimental findings. A closer look at Fig. 3(a) reveals two small recirculation zones at the foot of, respectively, the front and rear faces of the cube. The first zone is the consequence of a second stagnation point, since the downwash flow of the horse-shoe vortex meets the base wall. The second recirculation zone is a result of the arch vortex. A stagnation point is formed by the back flow (negative u-velocity) in the wake. Fig. 3(b) closely resembles the long-term-averaged imprint of surface streaks, obtained by surface oil visualisation of Meinders and Hanjalić (1999) (not shown here).

In the x–y plane very close to the base wall, at $z/h = 0.006$, in Fig. 3(b) one can see that the horse-shoe vortex in front of the obstacle is bent around the cube along the separation line. The convergence of the vortex with the upstream generated horse-shoe vortex takes place in the corridor region. The separation line at $x/h = 1.4$ in front of the windward cube face is directly related to the near-wall stagnation point. Moreover, on the side faces of the cube two small recirculation zones can be detected. These bubbles are produced by the separation of the flow from the sharp leading edges. The shear layer reattaches on the side walls at approximately $x/h = 2.2$. The streamlines in the wake show two counter-rotating foci, which point to two vortices perpendicular to the x–y plane. Together with the recirculation in the wake of Fig. 3(a) they form an arch-shaped vortex. Its location agrees reasonably well with the oil-film visualisation shown in Meinders and Hanjalić (1999). Note that the core flow in the region above the cube and in the streamwise corridors between the cubes remains almost undistorted.

Fig. 4 illustrates once more the main features of the flow structures. At location $x = 0$, $z/h = 0.3$ an array of 40 massless particles along the line $y/h = [1.5–2.5]$ is released. The pathlines are visualised in Fig. 4 from different view angles. The middle part of the particles

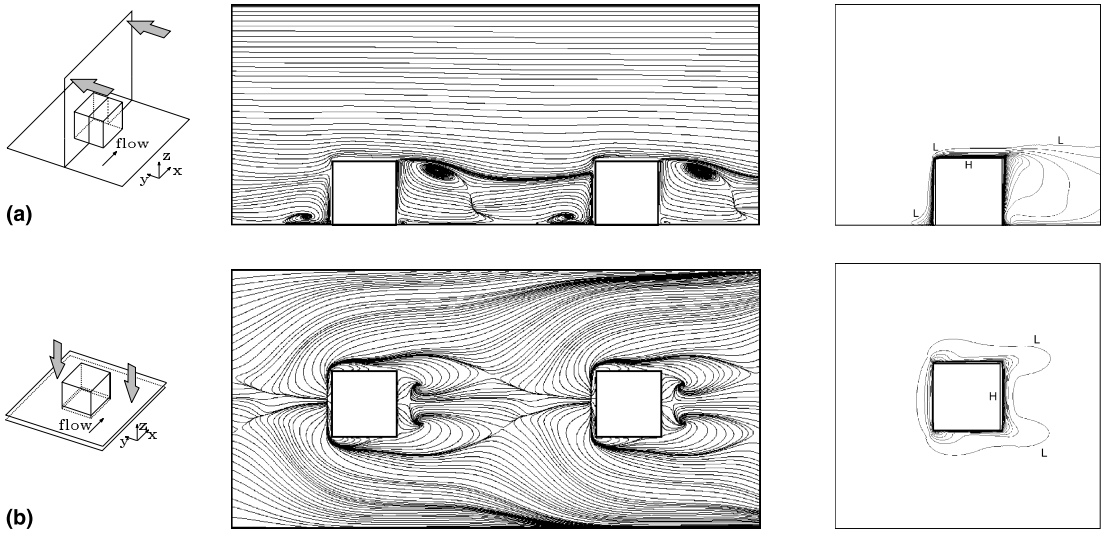

Fig. 3. Time-averaged streamlines of flow around the cube and corresponding temperature contours in the xz-plane at $y/h = 2.0$ (a) and in the xy-plane at $z/h = 0.006$ (b). Contour values: L: 20 °C, H: 55 °C, increment: 1 °C.

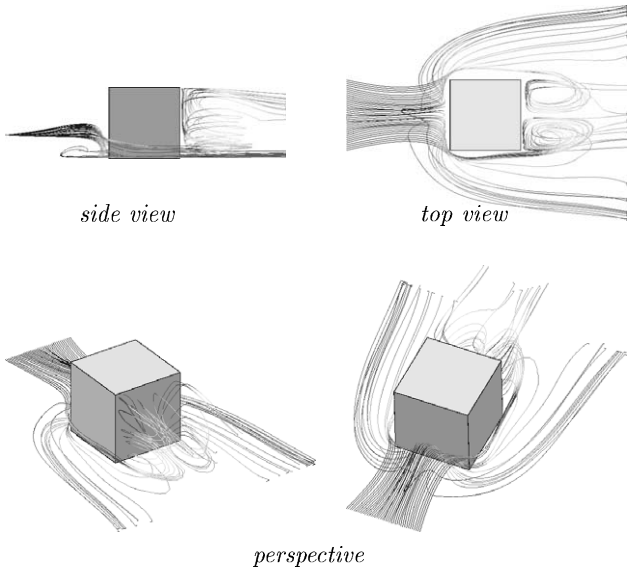

Fig. 4. Pathlines around cube of 40 particles injected along the line $y/h = [1.5–2.5]$ at location $x = 0,\ z/h = 0.3$.

($y/h = [1.8–2.2]$) is entrained into the horse-shoe vortex and is deflected downstream along both sides of the cube. The other part, from the starting point, $y/h = [1.5–1.8]$ and $y/S = [2.2–2.5]$, is transported alongside the shear layer. When these particles pass the downstream edges, they are sucked into the arch vortex in the wake. Due to the upward flow in the arch vortex, the particles are convected upwards where they meet the top shear layer and leave the domain. The particles are coloured with temperatures and the change of colour (here grey scales) indicates particle heating (red/light) when in contact or in the vicinity of the heated cube, and subsequent cooling (blue/dark).

A closer look at the arch-shaped vortex is provided in Fig. 5, in which an array of particles $y/h = [1.5–2.5]$ is injected into the flow at location $x/h = 4.0,\ z/h = 0.006$. The pathlines illustrate the negative velocity close to the base wall, which is a result of the recirculation zone in the wake. At $x/h = 2.7$ the particles meet the arch vortex, which transports them spirally upwards. Once they reach the upper shear layer, they are convected with it.

In addition to the streamline and particle pathlines, one can use vorticity to visualise coherent vortical structures, which quantify the local rotation of the flow. Fig. 6 shows the vorticity magnitude. Large vorticity concentrations are located in the near-obstacle wake directly behind the side faces, on the sides close to the leading edges and in front of the cube close to the base wall. These structures correspond closely to the vortex pattern discussed above. The coherent structures are the arch-shaped vortices, the recirculation bubbles at the sides of the cube and the horse-shoe vortex, respectively. A closer look at the wake recirculations shows that the arch vortex is not closed. Instead, the wake vortex in fact consists of three separate recirculations: the three vortices do not pair seamlessly into each other; they rather remain perpendicular to one other.

3.2. Instantaneous flow patterns

As discussed in the previous sections, the flow around the cube causes separations from all sides. In turbulent flow, instabilities are initiated at these locations causing the flow to fluctuate in a periodic manner in the form of periodic vortex shedding: vortices are periodically created and released from the edges. Though a turbulent flow is characterised by a broad spectrum of space and

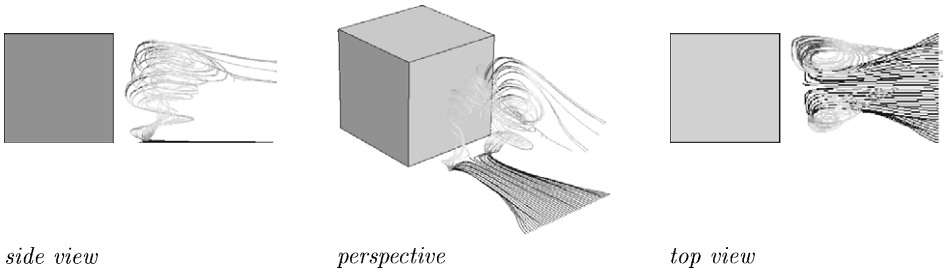

Fig. 5. Pathlines of 40 particles injected at location $x/h = 4.0,\ z/h = 0.006,\ y/h = [1.5–2.5]$.

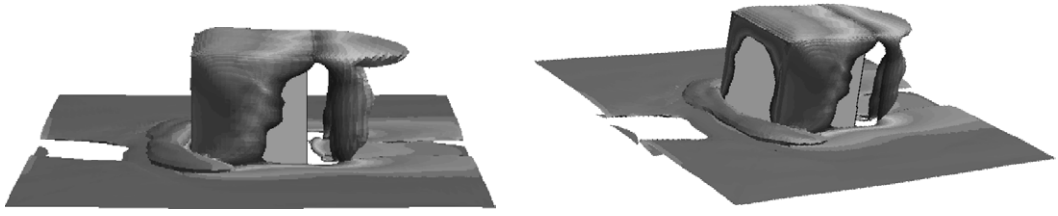

Fig. 6. Coherent structures visualised by vorticity magnitude at different perspective view angles.

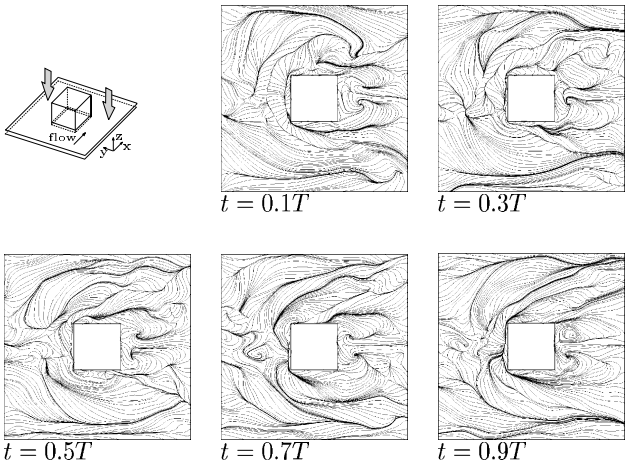

Fig. 7. Instantaneous streamlines around the cube at $z/h = 0.006$ at different time instants within one cycle.

time scales (frequencies), a dominant characteristic frequency can be derived from the maximum energy in the power density spectrum. For the Strouhal number $St = hf/U_0 = 0.109$, detected both by experiments and the present LES (obtained from time monitoring of the velocity at several locations), the cycle period corresponds to $T \approx 1000$ dimensionless time steps. Fig. 7 and 8 show a sequence of instantaneous streamlines on the planes $z/h = 0.006$ and $y/h = 2.0$, respectively, within one cycle, illustrating the time evolution of the vortical structures around the cube.

At time $t = 0.1T$ in Fig. 7 one can clearly detect the horse-shoe vortex in front of the cube. At $t = 0.3T$ the horse-shoe vortex asymmetrically breaks down due to instability and is dragged with the flow downstream along the cube ($t = 0.5T$). In the immediate proximity of the front of the cube a large stagnation region is formed ($t = 0.7T$), which causes a strong local advection of fluid along the sharp leading edges of the cube. This stagnation point and the strongly curved streamlines on both sides of the cube create a new horse-shoe vortex

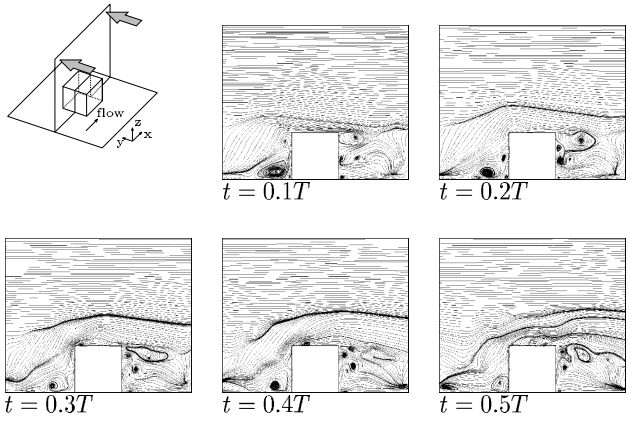

Fig. 8. Instantaneous streamlines around the cube at $y/h = 2.0$ at different time instants within one cycle.

($t = 1.0T$). From this sequence we can gather that the dominant characteristic flow frequency from Meinders and Hanjalić (1999) corresponds to the time development of the horse-shoe vortex, which is undoubtedly the largest and the strongest clearly detectable coherent vortical structure, as shown also above for the averaged field.

Fig. 8 shows the streamlines in the plane $y/h = 2.0$ at five time instants within the half of the main cycle. From this sequence one can see that the shedding frequency of the wake vortex is roughly twice as high as the dominant frequency. At $t = 0.1T$ in Fig. 8 we also observe next to the arch vortex small vortical nests in the wake of the cube. At $t = 0.2T$ the arch vortex is shed from the downstream cube edge and is replaced, i.e. pushed away by a smaller vortex. This vortex is advected upwards in the immediate proximity of the rear side of the cube by the upwash flow in the wake. The shed vortex is stretched between the upcoming and gradually growing vortex and the shear layer ($t = 0.3T$). Once the upcoming vortex has reached the downstream edge of the cube top, it is driven away by a new vortex, and so on ($t = 0.4T$, $t = 0.5T$).

3.3. Fluid velocity and temperature fields

Fig. 9 shows the contour plots of the normalised mean streamwise velocity U/U_0 and the normalised streamwise and spanwise Reynolds stresses $\overline{u'^2}/U_0^2$, $\overline{v'^2}/U_0^2$, respectively, in the vertical symmetry plane $y/h = 2.0$. The velocity plot shows clearly the regions of negative streamwise velocities. The Reynolds stresses indicate the level of fluctuation of the mean velocity components: they clearly show the anisotropy of the turbulent stress field, as discussed in the previous sections. The concentrations of streamwise fluctuations

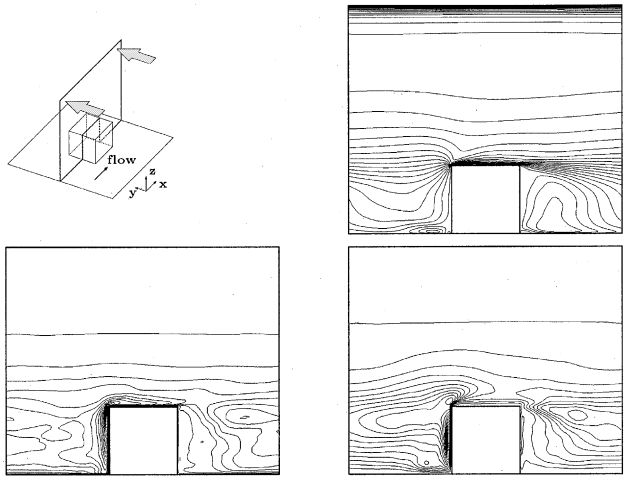

Fig. 9. Mean velocity U/U_0 and the Reynolds stresses $\overline{u'^2}/U_0^2$ (streamwise) and $\overline{v'^2}/U_0^2$ (spanwise) contours in vertical plane at $y/h = 2$.

$\overline{u'^2}/U_0^2$ in the horse-shoe vortex and bound top vortex underline both the high turbulence production and turbulence accumulation within these structures. The $\overline{v'^2}/U_0^2$ exhibits maxima in the impingement location of the flow on the front face, demonstrating the importance of the normal-to-the-wall velocity fluctuations in the enhancement of heat transfer.

Figs. 10–12 show the profiles of the normalised streamwise velocity U/U_0 and the normalised Reynolds stresses $\overline{u'^2}/U_0^2$ and $\overline{v'^2}/U_0^2$ at selected locations. Our results (full lines) and those of Ničeno and Hanjalić (1999) (dashed lines) are plotted together with the experimental results of Meinders (1998, 1999) (symbols). The latter were obtained using LDA with the experimental uncertainty of 5% for the mean velocities and 8% for the Reynolds stresses. Ničeno and Hanjalić (1999) performed the simulations with the same numerical code and mesh type, with a similar number of computational grid cells (418,760 cells) but with a stronger clustering towards the walls, aimed at positioning the first near-wall grid point at $y^+ \approx 0.5$. The mean velocity profiles of present simulations are generally in good agreement with experimental data. The results are also slightly better than those reported in Ničeno and Hanjalić (1999). Though a similar number of grid cells were used in Ničeno and Hanjalić (1999), due to stronger clustering towards the wall, the cells in the core region were coarser than in the computational grid used here. In the present study the grid distribution is regarded as more appropriate. The averaged temperature profiles in the cube mantle and in the fluid around the cube are illustrated in Fig. 13 around the cube circumference in the

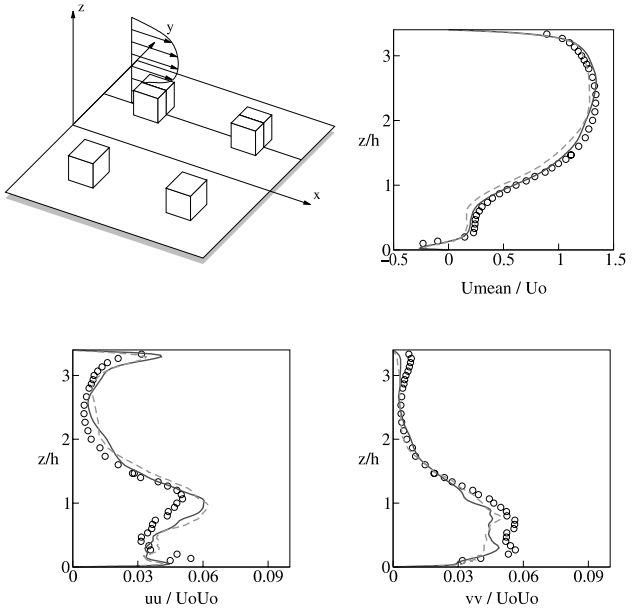

Fig. 10. Profiles in vertical plane at $y/h = 2$ and $x/h = 1.2$. Symbols: experimental results (Meinders, 1998); dashed lines: numerical result of Ničeno and Hanjalić (1999); solid lines: the present results.

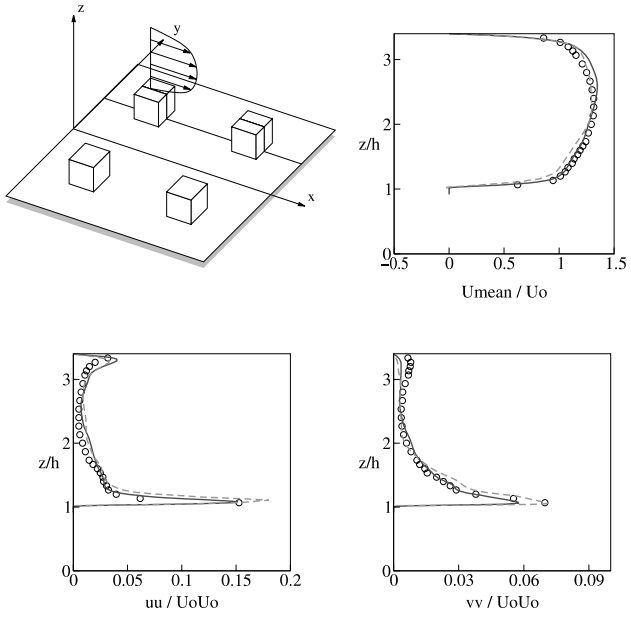

Fig. 11. Profiles in vertical plane at $y/h = 2$ and $x/h = 1.8$. For details see the caption of Fig. 10.

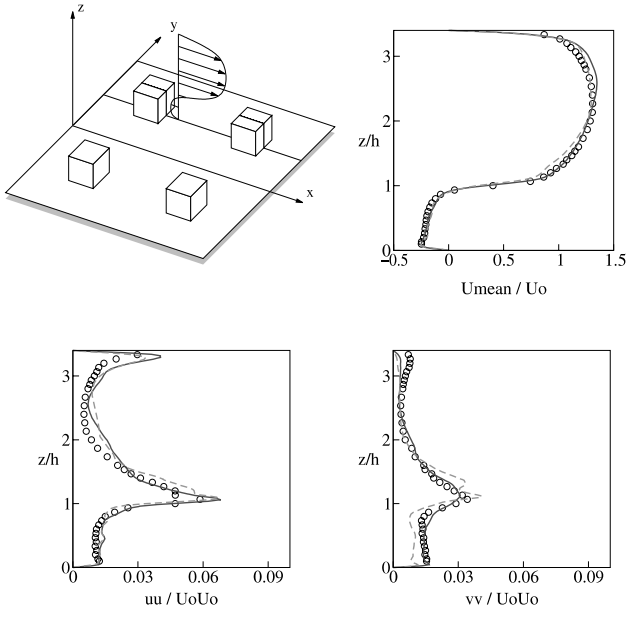

Fig. 12. Profiles in vertical plane at $y/h = 2$ and $x/h = 2.8$. For details see the caption of Fig. 10.

characteristic vertical mid-plane, showing a thin thermal boundary layer around the cube.

3.4. Cube surface temperature and heat transfer

3.4.1. Temperature profiles in characteristic mid-planes.

Prediction and analysis of the cube surface temperature and heat transfer distribution were the major goals of the present study. Experiments (Meinders and Hanjalić, 1999) provided liquid crystal and infrared

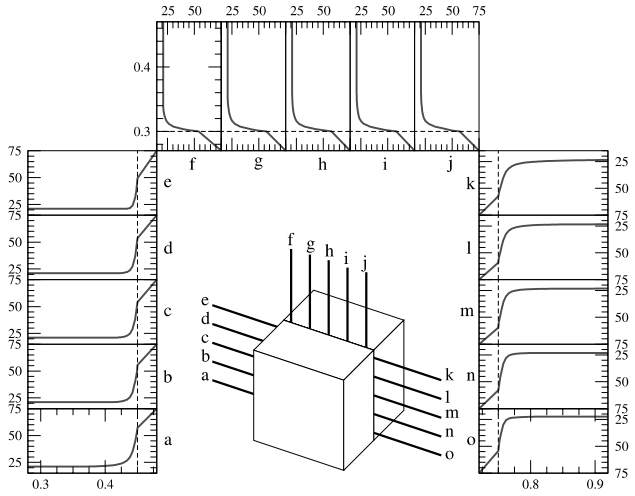

Fig. 13. Temperature boundary layer profiles in the vertical mid-plane ($y/h = 2$) and temperature distribution through the epoxy layer. Here $z_a/h = z_0/h = 0.1$, $z_b/h = z_n/h = 0.3$, $z_c/h = z_m/h = 0.5$, $z_d/h = z_l/h = 0.7$, $z_e/h = z_k/h = 0.7$, $x_f/h = 1.6$, $x_g/h = 1.8$, $x_h/h = 2.0$, $x_i/h = 2.2$, $x_j/h = 2.4$.

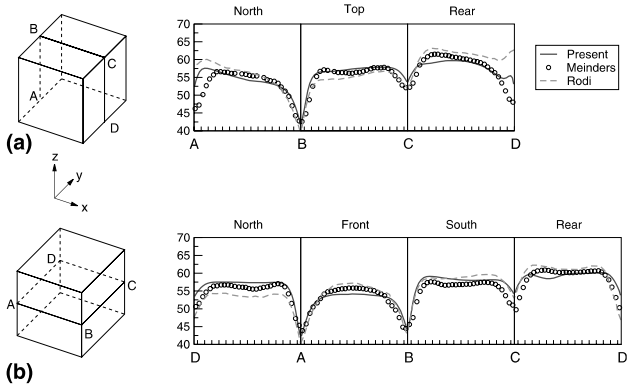

Fig. 14. Distribution of the surface temperature along, respectively, the path *ABCDA* in the horizontal plane (a) and the path *ABCD* in the vertical plane (b).

pictures of the surface temperature, but the detailed profiles have been reported only along the cube circumference in the characteristic mid-planes. In Fig. 14 the temperature profiles of both simulation results and experimental data are plotted. The results are in good agreement with the experiments (with an experimental uncertainty of 0.4 °C), except at the locations *A* and *D* in Fig. 14(b). The simulation predicts a higher surface temperature near the channel floor. These overpredictions are due to the fact that the unavoidable heat loss of the epoxy layer through the base wall was not modelled. The overpredictions are of the order of ~10%. This is in agreement with Meinder's findings (Meinders, 1998) that a conductive heat loss from the heated cube to the base plate was approximately 10%. The temperature profiles show a relatively uniform temperature over the central portion of each cube face, with steep gradients and minima at all cube edges, where the temperature drops by 8–15 °C (about 15–25% of the temperature in the central regions). This sharp decrease is a direct consequence of high local heat transfer rates, caused by intensive heat removal by high-speed fluid and flow separation. In view of the small size of the cube ($h = 15$ mm), such a strong temperature variation is a good indication of the complex vortex structure and of the possible danger of highly nonuniform cooling.

It is noted that in the experiment the cubes were actually mounted on a vertical wall. The full symmetry in the temperature distribution on the upper and bottom side faces (denoted as north and south) shown by experiments proves that the local buoyancy effects were negligible and that the problem can be regarded as pure forced convection. A slight asymmetry of the LES data is possibly the consequence of an insufficient number of realisations used for computing the averaged fields.

3.4.2. Flow structure imprint and temperature distribution on the cube surface

In order to further substantiate the role of vortical structure in the surface temperature distribution, we show in parallel the time-averaged structure imprints and the temperature field on the cube surface. Fig. 15

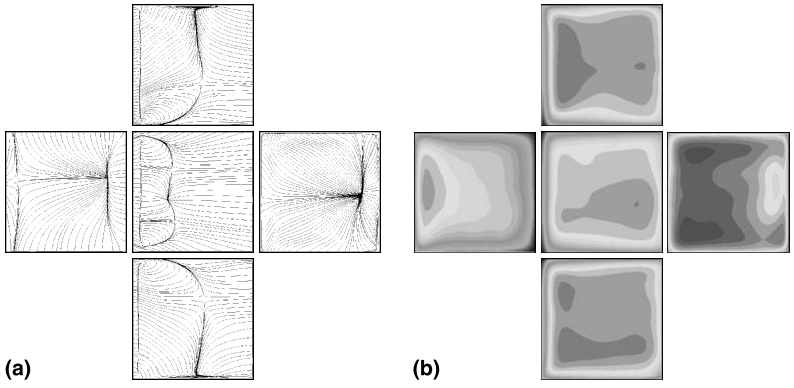

Fig. 15. Time-averaged streamlines on the five faces of the cube (a) and surface temperature map (b) of the cube in the matrix of cube arrangement. The flow is from left to right.

shows the near-surface streamlines (''streaks'') of the time-averaged flow and the isotherm maps on the five free faces of the cube respectively. The five faces are folded out and mapped into a plane. The flow is from left to right. The topology of the surface temperature plot shows a marked correlation with the streamline imprint. These should be compared with the temperature distribution along two pathlines in the horizontal and vertical planes respectively, given in Fig. 14. In the following we give a short discussion on the flow structure–temperature field correlation.

Front face. From the streamline plot, Fig. 15(a), one can observe the stagnation line at $z/h \approx 0.8$, caused by the flow impingement. This flow impingement caused a large convective heat transfer, which can be seen from Fig. 14 where the temperature profile at the front is significantly lower. Approaching the leading edges of the front side the profiles show a large decrease in the temperature. This region is characterised by high flow velocity: the fluid sweeps along the cube edges and removes the heat. Higher temperatures are found at the foot of the front face close to the channel wall. Since this region is dominated by the horse-shoe vortex, the induced flow recirculation prolongs the residence time of the fluid in the vortex. This allows the local fluid temperature to increase, and the vortex is, therefore, acting as a kind of insulation layer. This prevents the beneficial local convective heat transfer.

Top face. The temperature distribution on the top face shows a large spatial streamwise gradient: due to large velocity at the leading edge, the temperature is highly decreased. Though the imprint of the streamlines in Fig. 15 shows a small recirculation bubble on the top face, no significant temperature increase is seen at this location. This could be explained by the highly fluctuating character (vortex shedding) of this recirculation zone. Its characteristic frequency is much higher, but with a smaller amplitude than that detected in the horse-shoe vortex in front of the cube or in the vortex shedding area behind the cube. As a consequence, the trapped fluid has a very short residence time, resulting in an insignificant local fluid warming.

Rear face. The streamline plot of the rear face shows the stagnation point at approximately $z/h \approx 0.25$ from the base wall, indicating the impingement of the back flow on the wake. This recirculation is explained by the inward rotation of the wake vortex and the import of low-temperature fluid into the wake from the bottom. In the upwash flow at the rear face the fluid is heated, which results in a decrease of the local convective heat transfer. The local minimum in the temperature profile at the upper edge of the leeward face is explained by the presence of the shear layer, which convects cold air with it.

Side faces. The imprints of the streamlines on both side faces are practically symmetrical. In contrast, the temperature maps in Fig. 15(b) seem to be asymmetric. However, the temperature differences, according to the caption in Fig. 15(b), are rather small and could be explained by the fact that the flow (and conjugate temperature field) statistics were gathered over approximately only 35 periodic cycles. At the leading edges the flow separates and reattaches downstream on the side face at $x/h \approx 0.5$. As discussed in the previous section, these flow separations result in side vortices, which are oriented nearly parallel to the leading side edges. Analogue to the horse-shoe vortex, heat is entrapped in the side vortices, decreasing the convective heat transfer.

3.4.3. Instantaneous plumes and cube-surface temperature

As an illustration of the spatial and time nonuniformity of the instantaneous temperature field on and around the cube, we show some instantaneous snapshots of the temperature field, selected randomly. The pattern changes continuously with a stochastic periodicity and the illustration has only a qualitative character. Fig. 16 shows one realisation of the instantaneous surface temperature viewed from front and back of the cube surface (note that the same side face appears in both pictures). Although not regular, the pattern reflects the averaged surface temperature field shown in Fig. 15 and the flow structure: warm zones are visible in the lower part of the front face, just after the cube edge at the side face, and in the upper portion of the back face – all corresponding to local recirculation regions. Local hot spots are also discernible on the back face. The instantaneous fluid temperature, corresponding to the same realisation as in Fig. 16, is illustrated in Fig. 17. The figures show the thermal plume around the front and rear cube faces, represented by the surface of constant temperature – here 24.5 °C, and coloured by fluid velocity magnitude. Low fluid velocity (darker areas) are visible behind the cube corresponding to regions of low heat transfer, in contrast to high velocity (lighter areas) which corresponds to intensive heat removal from the cube.

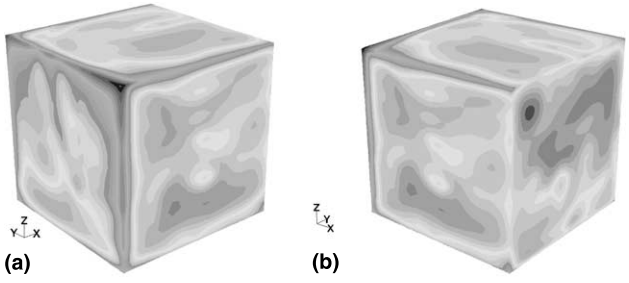

Fig. 16. Instantaneous temperature on the cube surface (random realisations): (a) view from front, (b) view from back.

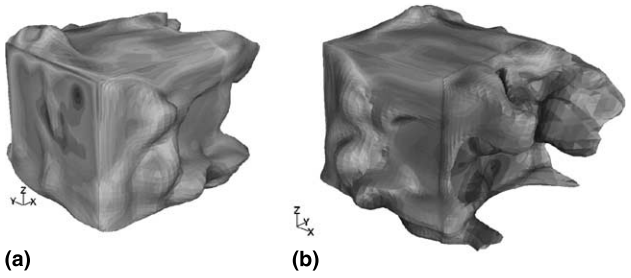

Fig. 17. Instantaneous plumes around the cube, represented by the surface of constant temperature – here 24.5 °C, and coloured by fluid velocity magnitude: (a) view from front, (b) view from back.

3.4.4. Averaged heat transfer on cube faces

Designers of electronics equipment are usually mainly interested in the total heat dissipation and heat removal from individual components. Although radiation and conduction through the base plate (made on purpose of finned, high-conducting slabs to act as a heat sink) play an important role, the convective heat removal usually poses the major uncertainty. Hence, the overall heat transfer coefficient is the major target of prediction methods.

We present here the averaged heat transfer coefficients obtained from the surface-integrated heat flux and surface temperature. Table 2 gives the numerical results of the face-averaged heat transfer coefficient at each cube face, together with the averaged heat transfer coefficient for the cube as a whole. The experimental data from Meinders (1998) are shown in the second column. These measurements were obtained with an experimental uncertainty of less than 10%. From Table 2 we can conclude that the simulations correspond remarkably well with experimental findings. As expected, the highest heat transfer coefficient is obtained for the front face and the lowest for the rear face. The difference between these two values is significant: the heat transfer on the front face is about 24% higher, and on the rear face 23% lower (in the experiment 30%) than the cube average. With a significant spatial nonuniformity, as shown in Figs. 15 and 14, the local surface temperature, even when considering the time-averaged values, may indeed depart from the cube mean temperature beyond the permitted limit, endangering the proper functionality of the equipment.

Table 2
Comparison of results for the mean heat transfer coefficient at each face

Cube face	$\overline{h}_{\mathrm{ref}}$	$\overline{h}_{\mathrm{ref}}$ [a]
Front	80.1	80.4
Top	65.6	65.5
Rear	49.6	45.0
Sides	62.9	66.7
Cube average	64.2	64.9

[a] Experimental data.

4. Conclusions

Convective heat transfer on a wall-mounted, internally heated multi-layered cube in a matrix has been computed using large eddy simulation (LES), with simultaneous computations of the temperature field in the low-conductive cube surface mantle. Detailed information was obtained about the instantaneous and averaged velocity and temperature in the fluid around the cube, as well as the temperature and heat transfer on the cube surfaces. In addition, the simulation provided a detailed insight into the vortical structure and turbulence field around the cube, and into their relationship with the cube surface heat transfer. The results are compared with experiments (Meinders and Hanjalić, 1999; Meinders, 1998) and LES on structured orthogonal mesh, reported in the literature (Mathey et al., 1999; Van der Velde et al., 1999). Several conclusions emerged from the present simulations, which are relevant to understanding the vortical structure and its relation to heat transfer on bluff bodies.

The calculated flow morphology around the cubes corresponds with that detected experimentally. It is characterised by a two-cell pattern in the space between the cubes, with a horse-shoe vortex on the windward face, an arch-shaped vortex in the wake of the cube, and bounded side vortices on the lateral sides and on top of the cube. The flow in the core region above the cubes and in the corridors between the cubes remains almost undistorted. These coherent structures were visualised by two-dimensional streamline plots and by three-dimensional particle pathlines and vorticity contours. From a sequence of instantaneous results, the periodic behaviour and the time development of the coherent structures are observed. The dominant frequency of the largest structure, i.e. the horse-shoe vortex, corresponds to the dimensionless characteristic shedding frequency of $St = 0.109$, very close to experimental findings. The shedding of the wake vortex was found to have approximately twice as high frequency as the dominant one. A quantitative comparison of the velocity profile and Reynolds stresses showed good agreement with experimental data.

The local heat transfer from the cube to the fluid is directly related to the coherent vortical structures in the direct proximity of the cube. The flow impingement on the front face and the flow separations from the sharp edges of the cube enhanced the heat transfer, while the detected recirculation zones prevent beneficial cooling. The highest temperatures are found on the rear wall of the cube, due to the presence of the arch-shaped vortex, which causes a long residence time of the fluid in the wake region. The averaged heat transfer coefficient on the front face is about 24% higher, and on the rear face about 23% lower than the cube averaged value. The temperature distribution on the cube surface is very

similar to experimental data. The profiles exhibit large spatial variation and steep gradients at the cube edges. The temperature was slightly overpredicted (~10%) in the near-base wall region – a consequence of discarding the experimentally detected heat loss through the base wall.

The use of an unstructured grid for the LES of flow and heat transfer on bluff bodies offers geometrical flexibility to fit bodies of arbitrary shape and to adopt a rational grid distribution with local refinement in areas with high fluid and flow property gradients. This in turn leads to a reduction of the total number of cells as compared with structured grids, and gives the possibility to handle complex geometries. The combination of these two features can significantly decrease the required number of grid points and, consequently, the computing time and memory.

As such, the LES on unstructured meshes, combined with simultaneous computation of conduction in solids, offers a viable route to predict all flow and heat transfer details in real applications, particularly at low and moderate Reynolds numbers, such as electronics cooling or the internal cooling of gas turbine blades. Of particular interest in such applications are the prediction of local overheating and hot spots, averaged and instantaneous, which can cause irreversible damage to equipment components and their technical failure. The results presented here show that detection of such local non-uniformity can easily be obtained by LES.

Acknowledgements

The work reported here has been sponsored by AVL-List GmbH, Graz, Austria. We thank Dr. B. Basara from AVL for monitoring the project and for the fruitful discussions and suggestions.

References

Baughn, J.W., Yan, X., 1992. Local heat transfer measurements in square ducts with transverse ribs. ASME HTD Enhanced Heat Transfer 202, 1–7.

Hanjalić, K., Obi, S. (Eds.), 1997. Proceedings, 6th ERCOFTAC/IAHR/COST Workshop on Refined Flow Modelling, June 6–7. Delft University of Technology, Delft, The Netherlands.

Hellsten, A., Rautaheimo, P. (Eds.), 1999. Proceedings, 8th ERCOFTAC/IAHR/COST Workshop on Refined Flow Modelling, June 17–18. Helsinki University of Technology, Helsinki, Finland.

Lasance, C.J.M., 1997. Status and challenges in thermal design of electronic parts and systems. In: Proceedings "Thermal Management of Electronic Systems". EUROTHERM Seminar No 58, September 24–26, Nantes, France, pp. 91–107.

Mathey, F., Fröhlich, J., Rodi, W., 1999. Flow in a matrix of surface-mounted cubes – Test case 6.2: description of numerical methodology. In: Hellstena, A., Rautaheimo, P. (Eds.), Proceedings, 8th ERCOFTAC/IAHR/COST Workshop on Refined Turbulence Modelling. Report 127, June 17–18. Helsinki University of Technology, Helsinki, Finland, pp. 46–49.

Meinders, E.R., 1998. Experimental study of heat transfer in turbulent flows over wall-mounted cubes. Ph.D. Thesis, Delft University of Technology.

Meinders, E.R., Hanjalić, K., 1999. Vortex structure and heat transfer in turbulent flow over a wall-mounted matrix of cubes. Int. J. Heat Fluid Flow 20, 255–267.

Ničeno, B., Hanjalić, K., 1999. Flow in a matrix of surface-mounted cubes – Test case 6.2. In: Hellstena, A., Rautaheimo, P (Eds.), Proceedings, 8th ERCOFTAC/IAHR/COST Workshop on Refined Turbulence Modelling. Report 127, June 17–18. Helsinki University of Technology, Helsinki, Finland, pp. 50–53.

Ničeno, B., Hanjalić, K., An unstructured finite-volume solver for large eddy simulations (submitted).

Piomelli, U., 1997. Large-Eddy Simulations: where we stand. In: Advances in DNS/LES, Proceedings of the First AFOSR International Conference on DNS/LES. Greyden Press, pp. 93–104.

Spalart, P.R., Jou, W.H., Strelets, M., Allmaras, S.R., 1995. Comments on the feasibility of LES for wings, and on a hybrid RANS/LES approach. Numer. Heat Transfer B 27, 323–336.

Van der Velde, R.M., Verstappen, R.W.C.P., Veldman, A.E.P., 1999. Description of numerical methodology for test case 6.2. In: Proceedings, 8th ERCOFTAC/IAHR/COST Workshop on Refined Turbulence Modelling. Report 127, June 17–18. Helsinki University of Technology, Helsinki, Finland, pp. 39–45.